Flow Turbulence Combust (2015) 94:527–554
DOI 10.1007/s10494-014-9589-6

An Experimental Study of Turbulent Non-Newtonian Fluid Flow in Concentric Annuli using Particle Image Velocimetry Technique

Majid Bizhani · Fabio Ernesto Rodriguez Corredor · Ergun Kuru

Received: 22 July 2014 / Accepted: 16 November 2014 / Published online: 4 December 2014

Abstract Turbulent flow of a Non-Newtonian polymeric fluid through concentric annuli is studied using a 9 m long horizontal flow loop (radius ratio = 0.4). The measurement technique used is Particle Image Velocimetry (PIV). The solvent Reynolds number is found to vary from 47000 to 66400. Pressure drops are measured and used to detect the onset of transition to turbulence. Measured velocity profiles are found to agree with the universal law of the wall for $y^+ < 11$. In the logarithmic region, however, velocity profiles deviate from log law, in a manner consistent with the flow of Newtonian fluids. Reynolds stress is found to be reduced significantly compared to water. The polymer is found to contribute significantly to the total stress close to the solid walls. The radii of maximum velocity are found to be biased toward the inner wall. Results of the turbulence intensity analysis show a slight increase of axial intensities in the buffer layer and especially around the outer wall of the annuli for polymer solutions. Radial velocity fluctuations are suppressed by means of polymer solution. The Root Mean Square (RMS) of vorticity fluctuation in the axial direction is also analyzed revealing a significant reduction of vortical activities as polymer is added to the flow.

Keywords Non-Newtonian fluid · Flow in annuli · PIV · Turbulent flow

1 Introduction

The flow of non-Newtonian fluids in annuli has a wide range of applications, such as oil and gas well drilling operation and heat exchanging devices. The behaviour of the

M. Bizhani · F. E. R. Corredor · E. Kuru (✉)
University of Alberta, Edmonton, Alberta, Canada
e-mail: ekuru@ualberta.ca

M. Bizhani
e-mail: Bizhani@ualberta.ca

F. E. R. Corredor
e-mail: fabioern@ualberta.ca

flow in annuli is different than in round tubes. In pipe flow symmetry requires the coincidence of the radial locations of zero shear stress and maximum velocity [1–3]. For pipe or channel flow total shear stress varies linearly with the distance from the wall. Flow in annular geometry, on the other hand, is not symmetric nor does the shear stress decay linearly with distance from walls. The laminar flow case has a theoretical solution for stress distribution [4, 5]. Although some investigators have sought to treat transitional and turbulent flow analytically [6, 7], the developed models are not universally accepted.

The volume of literature on the subject is considerable, but most studies have concerned flow of Newtonian fluids. Friction factor is one of the parameters of interest in most of these studies. For pipe flow the implicit Colebrook equation [8, 9] is well known and can be used to accurately predict friction factor. Compared to pipe flow, friction factors for flow in annulus have been reported to be slightly higher than for flow in a pipe of equivalent diameter [10–13]. Some studies even suggest that friction factor may be a function of radius ratio [10, 11] The Jones et al. correlation [14] which also accounts for radius ratio is widely accepted for Newtonian fluid flow in annulus. The non-Newtonian fluid flow in the annulus case, however, has received much less attention and there is no correlation available for friction factor in this case. While it is well known that polymer additives may cause a reduction in turbulent friction factor [15–17], the extent to which the friction factor is reduced depends on a number of parameters. Virk's ultimate asymptote [18], although developed for pipe flow, could be used to predict the maximum reduction in friction factor. For laminar regime Escudier et al. [16] have shown that the theoretical solution of Bird [19] is applicable for a power law type fluid. For cases other than laminar flow or condition of maximum drag reduction, friction factor correlation must be determined experimentally.

The transitional flow phenomenon in the annulus is also different than for pipe flow. A two stage transition has been reported in some studies [20]. Nouri et al. [15] carried out an experimental study of Newtonian and non-Newtonian fluids in annulus. Their results showed that the transitional flow regime occurs at higher Reynolds numbers for non-Newtonian fluids. In another study, Japper et al. [17] reported that transitional flow regime occurs over a wider range of Reynolds numbers for non-Newtonian fluids. Dou et al. [21] reported a dependency of critical Reynolds number on radius ratio

Coincidence of radius of zero shear stress and maximum velocity was an assumption in most of the early studies [12, 22, 23]. The results of studies by Lawn et al. [11] and Rehme [24] showed that the position of the zero shear stress occurred closer to the inner wall of the annuli than that of the maximum velocity. Results of Direct Numerical Simulation (DNS) of Chung et al. [25] also confirmed that the location of the zero shear stress was closer to the inner wall than that of the maximum velocity. Besides the issue of coincidence of the two radii, different studies suggest varying dependencies of these radii on the Reynolds number or radius ratio. In particular, some studies suggest that the radius of maximum velocity depends on the radius ratio [26], while others suggest it depends on the Reynolds number [23] Results of some investigators, however, have shown that, in fully developed turbulent or laminar flow the radius of maximum velocity is independent of both radius ratio and Reynolds number [20]. Hanks et al. [20] have reported a change in the radial location of maximum velocity in the transitional flow regime while it is fixed in the laminar and turbulent regime. Among the studies of non-Newtonian fluids, Nouri et al. [15] have examined a shear thinning polymer at Reynolds numbers of 1150 to 9600. Laser Doppler Anemometry (LDA) was used but within the experimental precision radius of zero shear stress and maximum velocity could not be distinguished from one another. Japper et al. [17] studied flow of three different non-Newtonian fluids in an annulus of radius ratio of 0.506.

Radius of zero shear stress and maximum velocity again could not be accurately distinguished from one another.

At this juncture, the velocity profile near the wall is also of great interest. Many investigations for both Newtonian and non-Newtonian fluids have shown that near solid surfaces the universal law of the wall applies [12, 16, 17]. For the area immediately adjacent to the near wall region, most studies concerned with Newtonian fluids have reported a logarithmic velocity profile similar to that of pipe flows [15, 17]. For non-Newtonian fluids, an upward shift in velocity profile has been reported in the logarithmic region [16]. Pinho [1] showed that velocity profiles of drag reducing fluids tend toward the Virk's [18] asymptote. The results of a study by Escudier et al. [16] also confirmed the upward shift in velocity profiles in the logarithmic region.

Due to difficulties in experimenting with turbulent flow especially in annulus, second order turbulent statistics have been the subject of interest in a few experimental studies [15–17, 27]. Among them, the experimental results of Rehme [27] have shown that axial turbulent intensities are somehow higher near the outer wall of the annulus. Results of the experimental work of Japper et al. [17] and DNS results of Chung et al. [25] also confirmed Rehme's conclusion. Other studies have also reported a drastic reduction in radial turbulence intensities and Reynolds stresses as polymer is added to the flow [15, 17]

In this paper, the results of an experimental study on the turbulent flow of polymer based fluids in horizontal annuli are presented and discussed. The working fluids are aqueous solutions of partially hydrolyzed poly-acrylamide (PHPA) prepared at two different polymer concentrations. A 2-D PIV technique is implemented in order to acquire instantaneous velocity field of turbulent flow along with pressure loss measurements. Friction factors are calculated and compared with different available correlations. The PIV data is analyzed to obtain the mean and fluctuating portions of the velocity field. Stress profiles are determined and results are compared with previous studies. Turbulence intensities in radial and axial directions are also compared with the results from the flow of Newtonian fluids.

2 Experimental Facilities

A schematic of the flow loop facility used in this study is shown in Fig. 1. The working fluids are prepared and stored in the tank. The capacity of the tank is 500 L, and is made of stainless steel. The mixer is air-driven and has adjustable speed. The fluid is pumped through the system by means of a centrifugal pump equipped with a Variable Frequency Drive (VFD), which is used to adjust the flow rate.

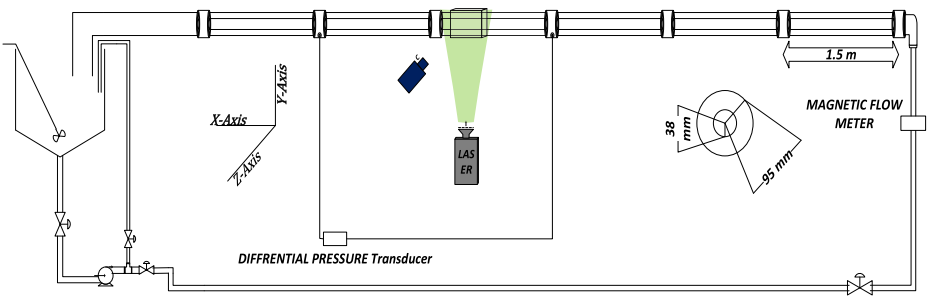

Fig. 1 Schematic of the flow loop

The test section is 9 m long, made of 6 Borosilicate glass pipes each 1.5 m in length with an inner diameter of 95 mm and a wall thickness of 5 mm. The refraction index of the glass pipes is 1.47. The stainless steel joints between the glass pipes have been specially designed with inner diameters identical to those of the pipes. The inner pipes are also made of glass, each 3 m in length with an outer diameter of 38 mm (The dimensions of the pipes are indicated in Fig. 1). To minimize sagging of inner pipe the thickness must be selected in such a way that results in near neutral buoyancy in the working fluid ([16, 17]). Inner pipes wall thickness is carefully selected to meet this condition in water based solutions. This reduces the tendency of inner pipes to bend upward or downward during experimenting [17] and therefore mitigating sagging and vibration. The annulus has a hydraulic diameter of 57 mm and a radius ratio of 0.4.

A magnetic flow meter installed at the inlet of the test section is used to measure the flow rates. The flow meter is a Ω OMEGA IS 2.140 with accuracy of ±0.5 %. Differential pressure loss is obtained from a pressure transducer (PX769) which has a range of measurement from 0 to 1490 Pa and accuracy of ±0.17 %. The transducer is located downstream of the inlet, at a distance from the annulus inlet sufficient to ensure that the flow is fully developed. All the measurement devices are connected to a computerized data acquisition system powered by LabView software. The pump RPM and, accordingly, fluid flow rate can be controlled by means of this software, which is also used to record all flow parameters such as pressure loss, temperature, and flow rate.

Velocity measurements are carried out at a distance of approximately $100D_H$ from the annulus' inlet to ensure the flow is fully developed; (a development length of $88D_H$ is required for obtaining a fully developed laminar flow [28], whereas turbulent flow develops at a shorter distance [17]). A rectangular box is designed and installed as an observation window (i.e., data collection window). The purpose of installing the rectangular box is to reduce laser light scattering due to the cylindrical shape of the glass pipes. Additionally, to reduce light refraction, the box is filled with glycerol (99 $\%Wt/Wt$ pure glycerol). Glycerol has a refraction index of 1.47, making it similar to glass pipes, which reduces refraction of light close to the outer wall of the annuli.

3 PIV Setup Description and Post-Processing Procedures

Generally a 2-D PIV setup consists of a light source and a recording device. The light source used in this study is a double pulse laser, and the recording device is a CCD double frame camera. The camera view is normal to the laser light as shown in Fig. 1; (in this figure, the camera view is along z-axis, and the laser light is lighting XY plane). By exposing tracer particles in the flow to laser light, they become visible to the camera and photographs of the flowing tracer particles can be taken. Double pulsed laser provides two separate illuminations of the flow within a very short period of time Δt. The CCD camera takes two photographs of the flow field during the two laser illuminations. Using the acquired pair of photographs, displacement of the particles can be evaluated and finally the instantaneous velocity vector is calculated.

The light source is a New Wave double-pulsed laser with a light wavelength of 532 nm. The thicknesses of beams vary between 0.5 mm and 3.5 mm; however, in this study the thickness is always kept at its minimum. This is due to the fact that thick light beams may result in errors in velocity measurements, especially when there is a big gradient across laser light thickness [29]. In this study, flow in the axial direction is of the greatest interest, whereas the gradient across laser light (along the z-axis in Fig. 1) is regarded as negligible.

A double-frame high resolution (1376×1040 pixels) CCD camera with two different lenses is used to capture photographs of the flow. The double framing feature of the camera allows for a pair of photographs to be taken within a very short period of time (Δt, which is adjustable and can be set as low as 500 ns). The time interval, Δt, depends upon the velocity and field of view of the camera, i.e., a higher velocity and smaller field of view necessitate a smaller Δt setting. During the experiments, two different lenses are used. For deep zooming and focusing on the near-wall region, a 60 mm Nikon AF Micro Nikkor with a 30 mm extension tube provides sufficient accuracy. For capturing the photographs of the entire flow field, a 50 mm Nikon AF Nikkor with a 12 mm extension tube is used.

The tasks of synchronizing the laser light beams with the camera frames, adjusting parameters such as Δt and laser light intensity, recording and storing the photographs, and post-processing the photographs are all completed using the DaVis 7.2 software provided by LaVision. More details pertaining to post-processing procedures are presented in the next section.

PIV technique relies on detecting displacement of tracer particles in the flow to obtain the flow field. Tracer particles in the flow scatter light upon incident with laser beams. The reflected light if has enough intensity (that depends on size and scattering characteristics of the particles) could be detected by the camera. In an accurate PIV imaging, to obtain sufficient spatial detail of the flow, concentration of tracer particles must be adequate [30]. Naturally occurring particles in the flow (e.g. impurities in tap water) are not sufficient for PIV imaging and therefore artificial seeding of the flow is necessary. LaVision has special seed particles for water based solutions. These particles are Glass hollow spheres with mean diameter of 10 μm and density of $1.1 \pm 0.05 \frac{g}{cc}$. In this study we have used the glass beads as seed particles for our PIV experiments.

4 PIV Data Post-Processing Procedures

After acquiring a pair of photographs of the seeded flow, the instantaneous velocity field can then be obtained. In the first step, an interrogation window of N×N pixels is chosen in the first image and, following this, a search region of the second photograph is examined for probable similarities. The Direct Cross Correlation Method (DCM) is applied to detect local similarities of brightness [31]. Those bright points showing the highest correlation are chosen as the destination of the same point in the first photograph. Particle displacement, Δs (Δx and Δy) can then be obtained. While the Δt (time between two photographs) is known, the instantaneous velocity must be calculated.

$$\begin{aligned} U &= \frac{\Delta x}{\Delta t} \\ V &= \frac{\Delta y}{\Delta t} \end{aligned} \tag{1}$$

For this study, 600 pairs of photographs of the flow obtained at a frame rate of 2.5 $frames/s$ are analyzed using the DaVis 7.2 software. First, interrogation window sizes of 64×64 pixels are chosen. In the second step, the size of the interrogation window is reduced to 32×32 pixels and again DCM is applied, although the vectors obtained in the first step are taken as offset values for the second step. The size of the interrogation windows and the overlapping of the multi-pass DCM are adjustable; sizes of 64×64 pixels and 32×32 pixels are chosen for the interrogation windows for the two respective steps, with 50 % overlap.

5 Preparation and Rheological Characterization of Test Fluids

A water soluble, anionic acrylamide-based copolymer (provided by Canamara United) is used as the additive to fresh tap water. The reported molecular weight of this polymer is$10 \times 10^6 \frac{g}{mol}$. Two concentrations of the polymer are tested (mass-based concentrations of 0.112 % and 0.129 % $\frac{wt}{wt}$, which correspond to 0.175 % & 0.2 % V/V % volumetric concentrations, respectively, using the reported density of the polymer powder to convert measured mass to volume). The solutions are prepared according to the supplier's recommendations. First, a concentrated batch is prepared by adding the polymer to water very slowly in order to avoid lumping while stirring at low RPMs to ensure that polymer degradation is not taking place. Then, water is added to the storage tank to dilute the fluid to the desired concentration. The fluid is allowed to rest for 45 minutes before the process of pumping it into the flow loop is begun. This allows those polymer molecules which have not already been dispersed to be dispersed in the solution, making the aqueous solution more homogeneous.

Following preparation of the solution, the fluid is pumped through the pipeline at the highest possible flow rate for 50 minutes prior to recording any data. The purpose of this step is to ensure the solution is homogeneously mixed. Once data acquisition is begun, samples of the fluid are taken at 10-minute intervals for rheology analysis to see if the fluid properties have changed. No significant changes in fluid properties are observed in any iterations of the experiment, (with the duration of each experiment kept as short as possible to avoid polymer degradation).

A Bohlin C-VOR 150 modular rheometer equipped with a spectrometer system which has a triple-mode motor control is used to measure the relationship between viscosity and shear rate. The rheometer allows for data to be collected both in controlled shear rate and controlled shear stress modes. In this study, all measurements are performed in controlled stress mode. Viscosity data are best fitted using the Carreau rheology model [19]. Equation 2 represents the fitted rheology model for 0.175 % polymer solution, while Eq. 3 represents the rheology model for 0.2 % polymer solution. Figure 2 illustrates the measured viscosity

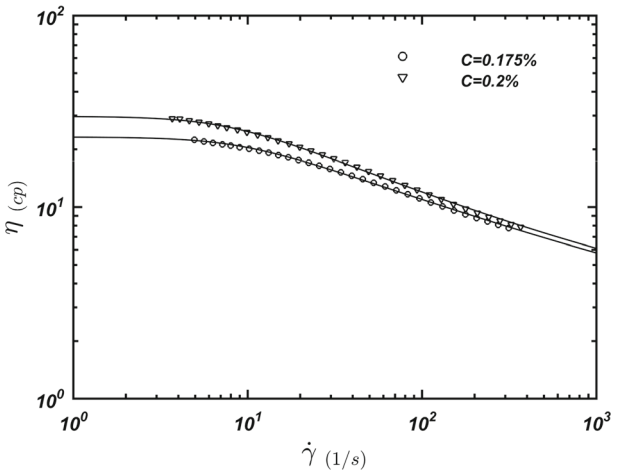

Fig. 2 Apparent viscosity versus shear rate

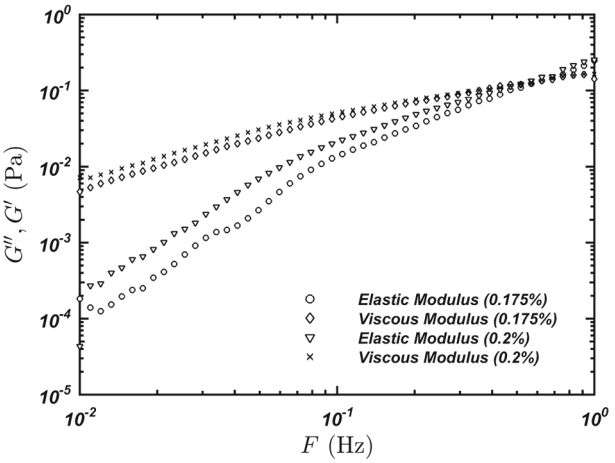

Fig. 3 Viscous and elastic modulus of the polymer solutions

data and fitted rheology models (Eqs. 2 and 3).

$$\frac{\eta - 1.5}{23.2 - 1.5} = (1 + (0.1096\dot{\gamma})^2)^{\frac{0.6541-1}{2}} \tag{2}$$

$$\frac{\eta - 2.25}{29.75 - 2.25} = (1 + (0.13\dot{\gamma})^2)^{\frac{0.5961-1}{2}} \tag{3}$$

Where $\dot{\gamma}$ is the shear rate ($\frac{1}{s}$) and η is the apparent viscosity (cp).

The density of the fluids is assumed to be the same as that of the solvent (water). This assumption is justified based on the very low concentrations of the polymers. The liquid is also homogeneously mixed, which implies there is no density gradient anywhere in the flow.

Oscillatory rheometry measurements are also taken to measure viscoelastic properties of the polymer solutions. Figure 3 shows the elastic (storage) modulus and viscous (loss) modulus of the two fluids. The phase angle is also reported in Fig. 4, where a phase angle

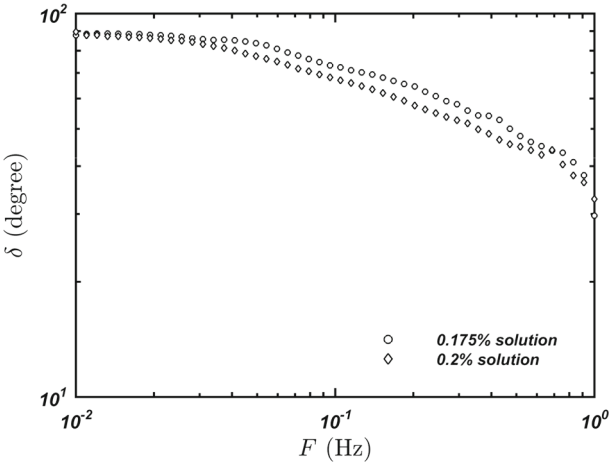

Fig. 4 Measured phase angle versus frequency

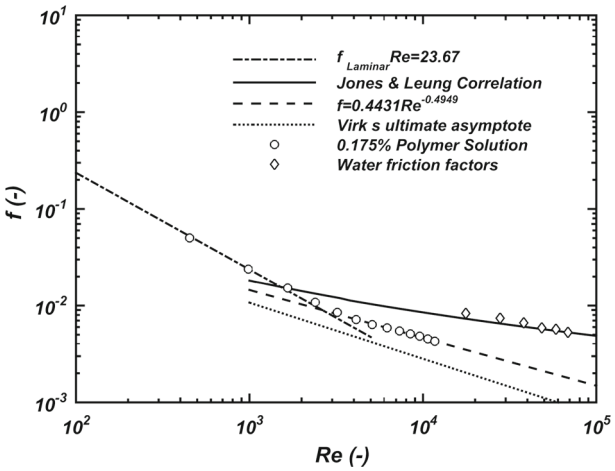

Fig. 5 **f** − **Re** Data for 0.175 % polymer solution

of 90° corresponds to a pure viscous material. A pure elastic material has a phase angle of 0°. As shown in Fig. 4, for small frequencies (i.e., large time scales) both fluids behave like pure viscous fluids. As frequency increases, the phase angle decreases, which indicates that polymer solutions become more elastic at smaller time scales. It is also worth mentioning that the fluid with a higher polymer concentration is slightly more elastic.

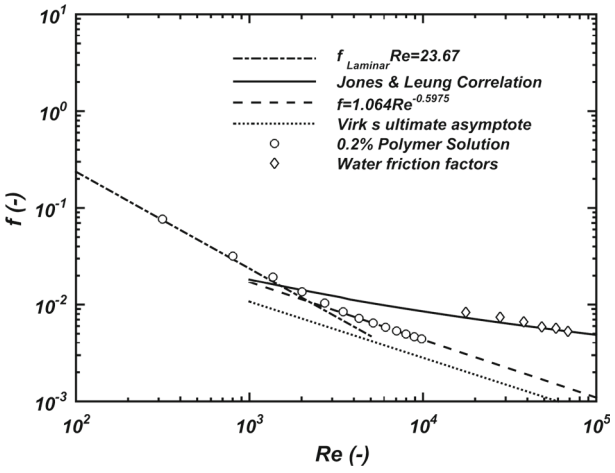

Fig. 6 **f** − **Re** Data for 0.2 % polymer solution

6 Results and Discussion

6.1 Frictional pressure drop measurement and identification of flow regime transition

Fanning friction factor versus Reynolds number data for flow of the two aqueous polymer solutions are plotted in Figs. 5 and 6. It should be noted that all three flow regimes are encountered. In the laminar flow regime the data closely follows the Newtonian fluid friction factor line represented by Jones' correlation [14] (for a radius ratio of 0.4):

$$f.Re = 23.67 \tag{4}$$

Where f represents the fanning friction factor calculated using the weighted average of wall shear stress [16]

$$f = \frac{2\tau_A}{\rho U_B^2} \tag{5}$$

$$\tau_A = \frac{1}{4}\left(D_o - D_i\right)\frac{dP}{dx} \tag{6}$$

U_B is the bulk velocity, D_o is the inner diameter of the outer pipe, D_i is the outer diameter of the inner pipe, τ_A is the weighted average wall shear stress, and $\frac{dP}{dx}$ is the measured frictional pressure loss.

The Reynolds number is based on the hydraulic diameter and viscosity at the wall, as shown in Eq. 7 [15].

$$Re = \frac{\rho U_B D_H}{\eta_w} \tag{7}$$

D_H is the hydraulic diameter defined as $D_o - D_i$.

As the Reynolds number increases, the friction factor data begins to deviate from the laminar flow line. A clear reduction in friction factor is observed in the turbulent flow regime compared to the friction factor for turbulent water flow (calculated using the Jones and Leung correlation for turbulent flow regime (Eq. 8, [14]).

$$\frac{1}{\sqrt{f}} = 4\log 1.3514 Ref^{\frac{1}{2}} - 1.6 \tag{8}$$

Reduction in friction factor is a typical behavior of polymer-based fluids. In Figs. 5 and 6, turbulent friction factors are also compared with Virk's ultimate asymptote of drag reduction curve. This relation, as in Eq. 9 (limited for $4000 < Re < 40000$), pertains to pipe flow and represents the friction factor for the condition of maximum drag reduction.

$$f = 0.59 Re^{-058} \tag{9}$$

Measured friction factors for both polymer solutions lie within the window enclosed by the Newtonian fluids curve (8) and Virk's equation (9). The turbulent friction factor for the first polymer solution best matched the following correlation obtained by curve-fitting the last 8 points of the data presented in Fig. 5.

$$f = 0.4431 Re^{-0.4949} \tag{10}$$

Similarly, turbulent friction factor of a 0.2 % polymer solution follows Eq. 11 (obtained by curve-fitting the last 7 points of the data in Fig. 6).

$$f = 1.064 Re^{-0.5975} \tag{11}$$

Similar to the results of Nouri et al. [15] and Pinho et al. [1], the friction factor data shows that the transition from laminar to turbulent flow occurs at a higher Reynolds number

Table 1 Bulk velocities, Reynolds, and solvent Reynolds numbers of PIV experiments

	C=0.175 %	C=0.2 %	Solvent Reynolds number
$U_B\ (\frac{m}{s})$	$Re(-)$	$Re(-)$	$Re_s\ (-)$
0.827	7700	5800	47000
1	9300	7500	57000
1.16	11200	9200	66400

than for Newtonian fluids. Onset of the transition to turbulence for a Newtonian fluid is reported to be at $Re = 2100$ [17]. The data in Figs. 5 and 6 shows that, for polymer fluid flow, transition occurs at Reynolds numbers exceeding approximately 3,000. A delay in transition to turbulence causes suppression of turbulence in the flow of shear thinning fluids [1], a scenario which will be addressed in greater detail in the discussion of the turbulence statistics analysis.

While the primary purpose of this study is to investigate turbulent flow of Non-Newtonian fluids, determining the velocities, which would ensure turbulent flow regime, is found to be a challenging but necessary task. Based on the information obtained from $f-Re$ data and considering the limitation of the pump capacity, three velocities are selected for experimenting with PIV. These velocities, along with the corresponding Reynolds numbers and corresponding solvent Reynolds numbers, are reported in Table 1. The solvent Reynolds number is defined as follows:

$$Re = \frac{\rho U_B D_H}{\eta_s} \tag{12}$$

Where η_s is the viscosity of the solvent, which in this case is water.

6.2 Velocity profiles

Velocity profiles close to solid walls are measured using the PIV technique. To obtain the maximum number of data points within the boundary layer, a 60 mm lens and a 30 mm extension tube are used. To transform the measured velocity data into wall units (i.e., y^+ and u^+) the wall shear stresses on each wall of the annuli must be determined. The wall shear stresses on inner wall and outer wall are not equal, as shown in Eqs. 13 & 14 [15].

$$\tau_i = -\left(\frac{dp}{dx}\right)\left(\frac{R_0^2 - R_1^2}{2R_1}\right) \tag{13}$$

$$\tau_o = -\left(\frac{dp}{dx}\right)\left(\frac{R_2^2 - R_0^2}{2R_2}\right) \tag{14}$$

Where R_1 is the outer radius of the inner pipe, R_2 is the inner radius of the outer pipe and R_0 is the radius at which shear stress is zero. Due to the lack of information about total shear stress, the radius of zero shear stress cannot be accurately determined. Therefore, in place of the radius of zero shear stress the radius of maximum velocity is used in this study. Once the proper wall shear stress is calculated, Eqs. 15, 16, and 17 can be used to transform the data into wall units.

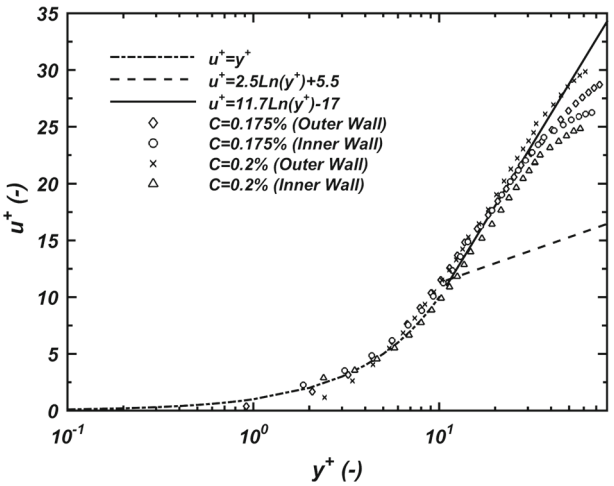

Fig. 7 Near-wall velocity data in wall unit for $\mathbf{Re_s}$= **47000**

$$u_\tau = \sqrt{\frac{\tau_w}{\rho}} \tag{15}$$

$$u^+ = \frac{\bar{u}}{u_\tau} \tag{16}$$

$$y^+ = \frac{\rho y u_\tau}{\eta_w} \tag{17}$$

The velocity profiles in the wall units are shown in Figs. 7, 8, and 9. Velocity data closely follow the universal law of the wall (18) within the viscous sublayer (near the wall region).

$$u^+ = y^+ \tag{18}$$

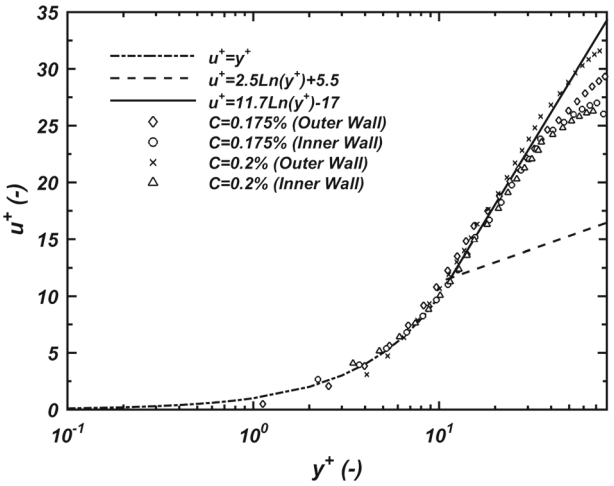

Fig. 8 Near-wall velocity data in wall unit for $\mathbf{Re_s}$= **57000**

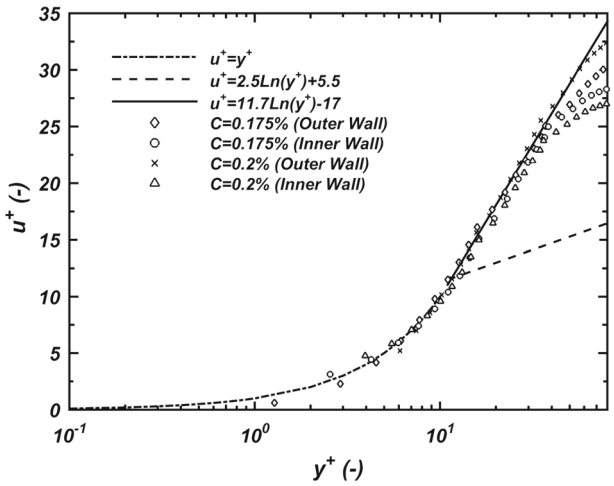

Fig. 9 Near-wall velocity data in wall unit for $\mathbf{Re_s} = \mathbf{66400}$

The nearwall region extends to a dimensionless distance (y^+) of 11. Regardless of the type of fluid, the wall (inner versus outer) and the Reynolds number, the velocity profile obeys this law for $y^+ < 11$

For $y^+ > 11$, velocity profiles of polymer fluids do not conform to the logarithmic relationship of Newtonian fluids expressed in Eq. 19 [32].

$$u^+ = 2.5 \ln\left(y^+\right) + 5.5 \tag{19}$$

In this region, there is an upward shift in the polymer fluid velocity profiles, marking a deviation from Newtonian fluid velocity profile. This behaviour of velocity is associated with the drag reduction properties of the polymer solutions. The velocity profile for $y^+ > 11$ tends to shift towards the Virk's asymptote of maximum drag reduction [18] (20).

$$u^+ = 11.7 \ln\left(y^+\right) - 17 \tag{20}$$

To obtain the velocity distribution from the inner wall to the outer wall of the annuli, the existing lens is exchanged for a 50 mm Nikon. The resultant velocity profiles are plotted in Fig. 10. The result for flow of water is included for comparison purposes [32]. To mark the difference in shape of velocity profiles, velocity data are presented in dimensional form.

Dimensionless radial locations of maximum velocities are determined using the data presented in Fig. 10. The location of maximum velocity is determined from curve-fitted velocity profiles obtained using a MATLAB curve-fitting tool (see Table 2). Results for flow of water are also included for comparison purposes [32]. Within the experimental level of precision, maximum velocity is found to occur closer to the inner wall of the annuli. Also, the radius of maximum velocity is smaller for water than for polymer solutions. Generally, as polymer concentration increases, this radius also increases (i.e., moves away from the inner wall). The Reynolds number does not affect the position of maximum velocity for flow of water and lower polymer concentrations. For 0.2 % solution, however, the data is scattered and this conclusion cannot be verified.

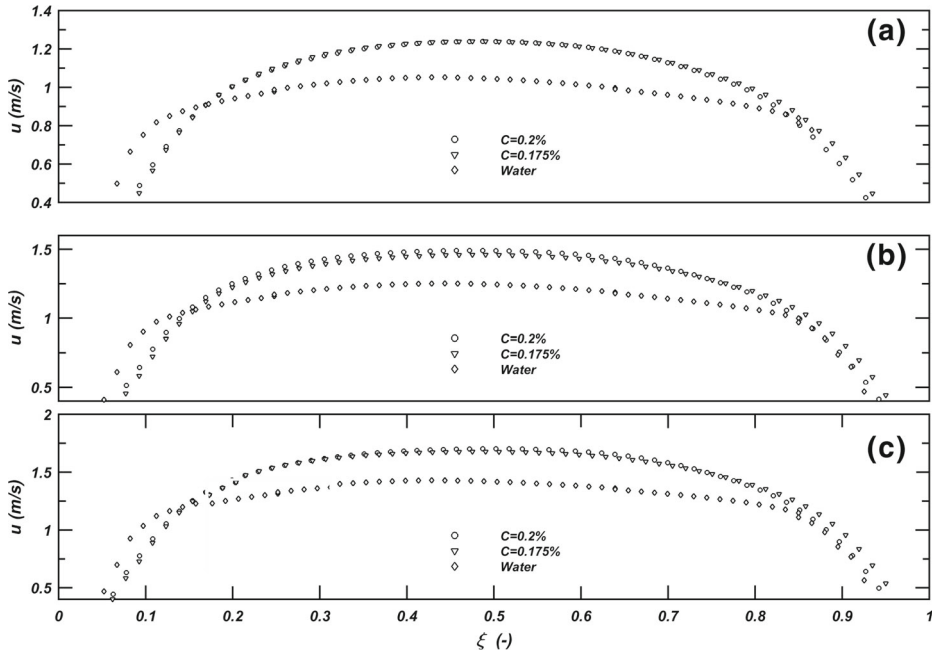

Fig. 10 Velocity Profiles in Whole Annular Gap (a) $\mathbf{Re_s}$= **47000** (b) $\mathbf{Re_s}$= **57000** (c) $\mathbf{Re_s}$= **66400**

6.3 Shear stress

Reynolds stress by definition is the product of density and the time average of fluctuation components of the velocity (21).

$$\tau_{Re} = -\rho \bar{u'v'} \tag{21}$$

PIV measurements primarily provide the instantaneous velocity profiles. By applying the Reynolds decomposition procedure to PIV data, one would be able to obtain time average and fluctuation components of the velocity. Results of Reynolds stress calculations for the two polymer solutions are reported in Figs. 11, 12, and 13.

A comparison of the stress profiles reveals that at the same bulk velocity, the Reynolds stress is much higher for water than for the polymer solutions. In fact, compared to water, polymer's turbulent stress is almost negligible. For the higher polymer solution (0.2 %), Reynolds stresses are nearly zero throughout the entire cross section, similar to Warholic results [36]. The primary cause of Reynolds stress reduction is the reduction of radial velocity fluctuation caused by polymer molecules [33]. Another reason is the effect of Reynolds number on the Reynolds stresses. Reynolds stress indicates the contribution of turbulence

Table 2 Dimensionless radial location of maximum velocity for water and 2 polymer solutions

	Water	C = 0.175 %	C = 0.2 %
Reynolds Number	$\xi(-) = \frac{R_{max}-R_1}{R_2-R_1}$		
Re_s = 47000	0.43	0.45	0.46
Re_s = 57000	0.44	0.45	0.44
Re_s = 66400	0.43	0.45	0.47

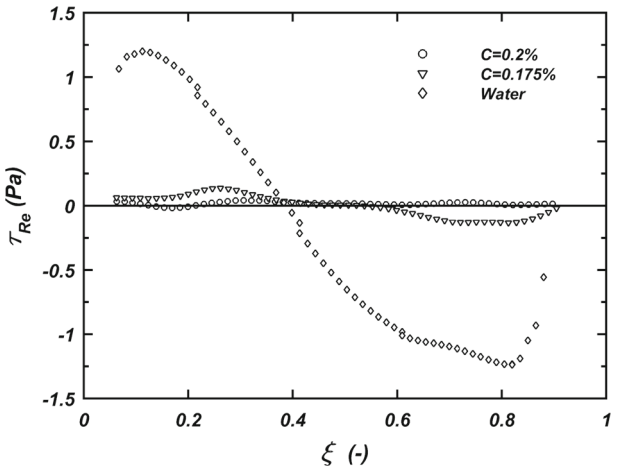

Fig. 11 Reynolds stress profile at $\mathbf{Re_s = 47000}$

to the total stress, and it becomes lower as the Reynolds number decreases. Previous studies on the drag reduction phenomenon also suggest a drastic reduction of Reynolds stresses by adding polymer to the flow [15, 17, 34, 36, 40].

Total shear stress in turbulent flow is the summation of three separate stresses as expressed in Eq. 22 [35]:

$$\tau = \tau_{Re} + \tau_s + \tau_p \tag{22}$$

In Eq. 22, τ_{Re} is the turbulent or Reynolds stress as defined earlier; τ_s is solvent stress and is defined as follows:

$$\tau_s = \eta_s \frac{du}{dy} \tag{23}$$

Where η_s is the viscosity of the solvent.

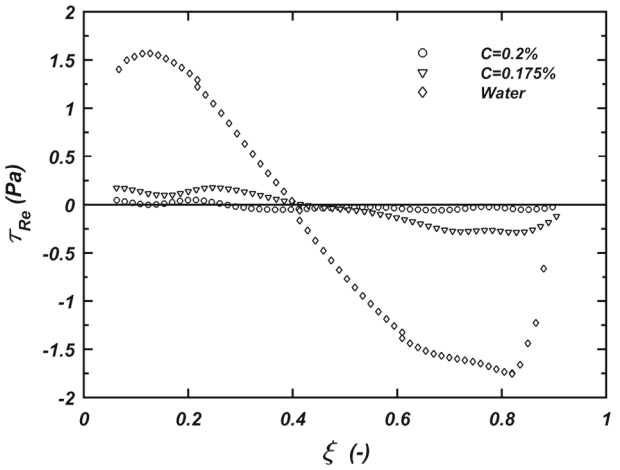

Fig. 12 Reynolds stress profile at $\mathbf{Re_s = 57000}$

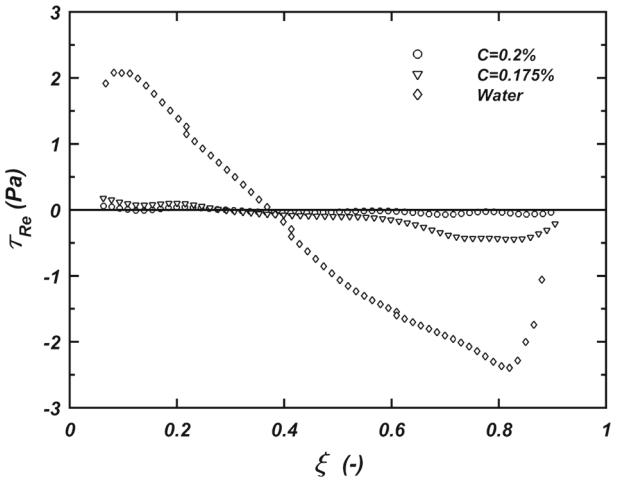

Fig. 13 Reynolds stress profile at $\mathbf{Re_s} = \mathbf{66400}$

The third component in the total stress equation τ_p is the polymer stress. This component has a value of zero for the flow of a Newtonian fluid. Indeed polymer stresses arise from the elastic properties of these fluids [40]. The case in which the summation of the solvent and Reynolds stresses is not equal to the total stress for viscoelastic fluids is referred to as "stress deficit" [35].

In order to quantify the stress deficit knowledge of total shear stress and the other two components of the total stress are required. In the case of pipe flow, total shear stress can be calculated using the decay law (shear stress decays linearly with distance from the pipe wall). Therefore if the Reynolds and solvent stresses are measured an estimate of the work done by the polymer molecules can be obtained [35]. The same arguments also apply for channel flow where shear stress varies linearly with distance. In the case of flow in the

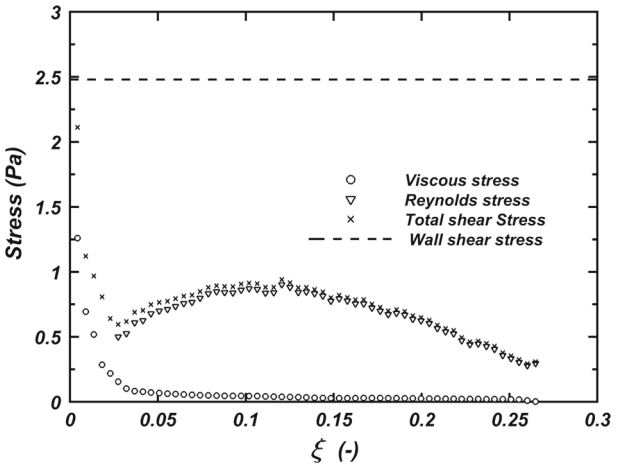

Fig. 14 Contributions of different components of total stress for flow of water at $\mathbf{Re} = \mathbf{47000}$ near inner wall

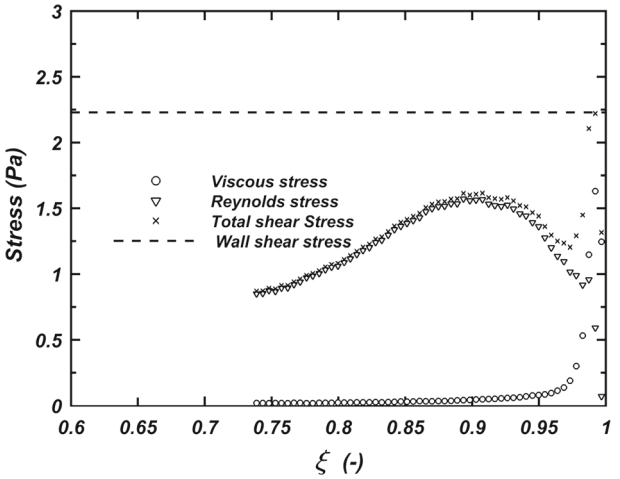

Fig. 15 Contributions of different components of total stress for flow of water at **Re = 47000** near outer wall

annulus, neither does the shear stress decay linearly nor is there a theoretical solution applicable for a total shear stress profile in a fully turbulent flow. The only points where the total shear stress is known are on the walls. In fact wall shear stress calculated using pressure loss measurements (Eqs. 13 and 14) represents total shear stress at solid walls

Polymer stress is caused by elastic behavior of polymer molecules. It is therefore expected that τ_p in Eq. 22 will be reduced to zero in the case of a Newtonian inelastic fluid. In Figs. 14 and 15, two components of the total stress (Reynolds and solvent) are computed for flow of water which represents a Newtonian inelastic fluid. The corresponding wall shear stress calculated using Eqs. 13 and 14 is also shown in the figures. Clearly for most parts of the near wall solvent stress is negligible. However a sharp increase is observed close to the walls. Summation of solvent and Reynolds stress (which is called total stress in the case

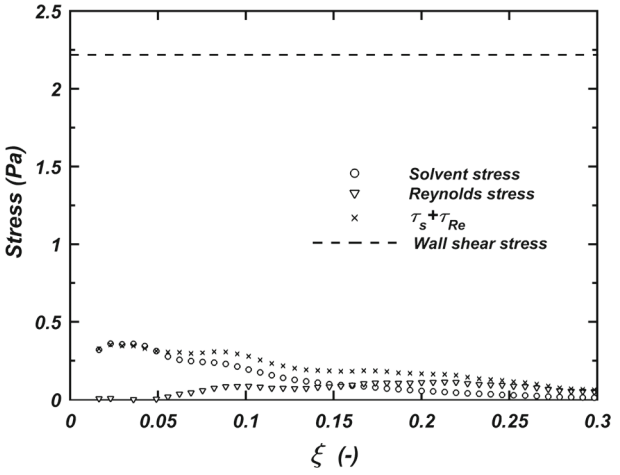

Fig. 16 Contributions of different components of total stress for flow of 0.175 % polymer at $\mathbf{Re_s}$= **47000** near inner wall

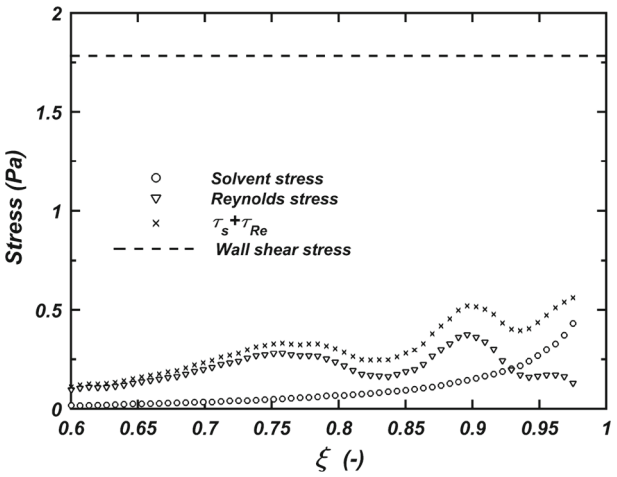

Fig. 17 Contributions of different components of total stress for flow of 0.175 % polymer at $\mathbf{Re_s = 47000}$ near outer wall

of water) is also plotted. Both Figs. 14 and 15 show that total shear stress tends toward the actual wall shear stress computed from the pressure drop data as walls are approached. This means that the polymer stress is indeed zero which is the expected result for water. The data from water flow is analyzed to show the accuracy of the method which confirms that the same analysis can be applied for polymer solutions.

In an attempt to quantify the contribution of polymer stress to total stress, the summation of solvent and Reynolds stress for the low concentration polymer solution is plotted and compared to total shear stress at the walls. In Figs. 16, 17, 18, 19, 20 and 21 the Reynolds, solvent and wall shear stresses for 0.175 % polymer solution are reported. As seen from these figures, Reynolds stresses are greatly reduced but they are still non-zero (Similar

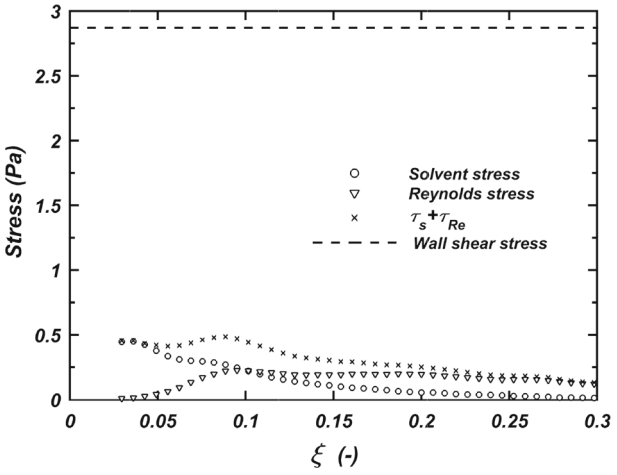

Fig. 18 Contributions of different components of total stress for flow of 0.175 % polymer at $\mathbf{Re_s = 57000}$ near inner wall

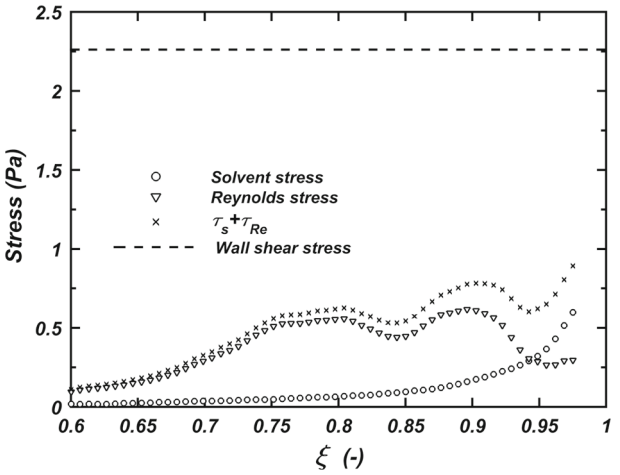

Fig. 19 Contributions of different components of total stress for flow of 0.175 % polymer at $\mathbf{Re_s = 57000}$ near outer wall

results have also been reported by Ptasinski et al. [34, 35]) Contrary to with water, solvent stress and Reynolds stress are in the same range for the polymer solution. Finally a significant difference is observed between the wall shear stress and the sum of Reynolds stress and solvent stress. This is attributable to the effect of the polymer and the difference is the polymer stress at the walls. Previous studies have shown that polymer stress can contribute up to 60 % of total stress [35]. Results of DNS work by Min et al. [40] have shown polymer stress increases as Reynolds number increases. The results of our study have also shown polymer stress to make a significant contribution to total stress. It is also interesting to note that the stress deficit is higher for the inner wall than for the outer wall (Figs. 16, 17, 18, 19, 20 and 21).

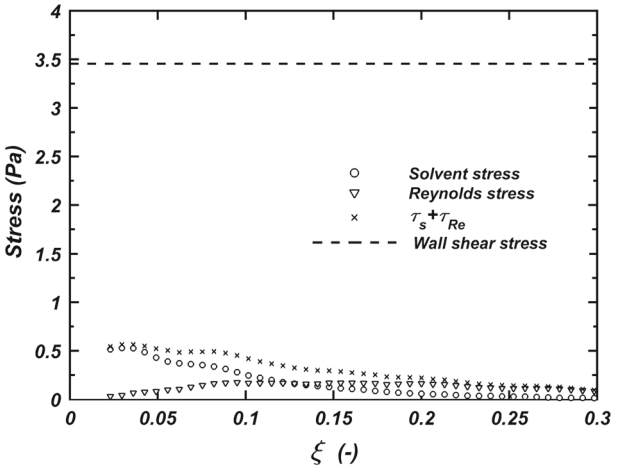

Fig. 20 Contributions of different components of total stress for flow of 0.175 % polymer at $\mathbf{Re_s = 66400}$ near inner wall

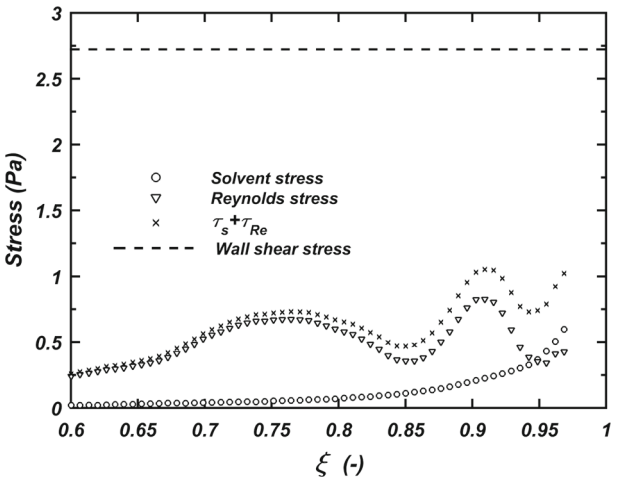

Fig. 21 Contributions of different components of total stress for flow of 0.175 % polymer at $\mathbf{Re_s = 66400}$ near outer wall

For all second order turbulence statistical analyses, it should be noted, the results of the lower concentration of polymer (0.175 %) are used.

6.4 Turbulent intensities

6.4.1 Axial intensities

Axial turbulence intensity by definition is the RMS (Root Mean Square) of the fluctuation velocity in the axial direction. To normalize the intensities, the friction velocity is used.

$$u^+_{rms} = \frac{U_{RMS}}{u_\tau} \tag{24}$$

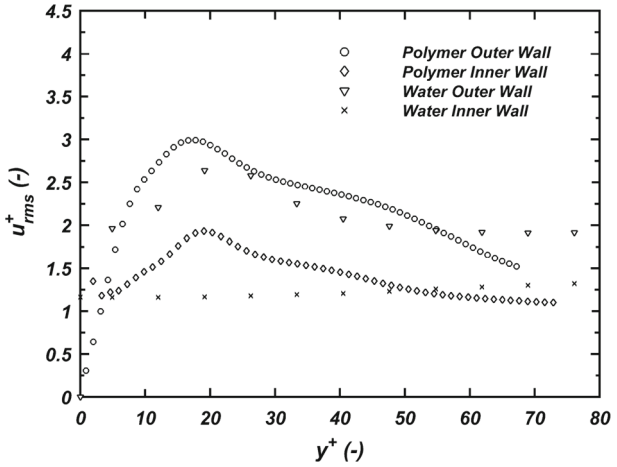

Fig. 22 Axial intensity profile at $\mathbf{Re_s = 47000}$

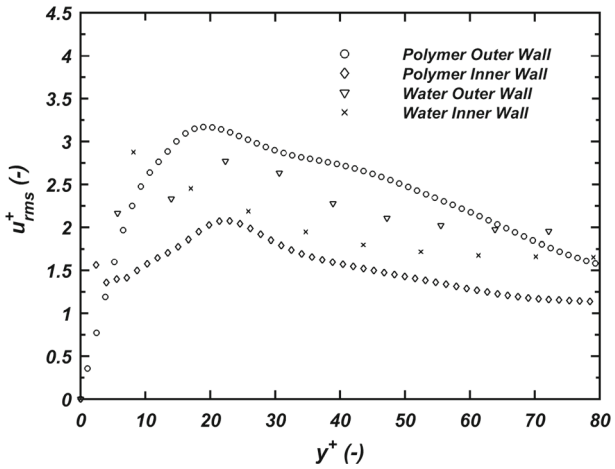

Fig. 23 Axial intensity profile at $\mathbf{Re_s} = \mathbf{57000}$

Measured values of axial intensities for the 0.175 % concentration and for water are reported in Figs. 22, 23, and 24. Very close to the walls ($y^+ < 11$), water seems to have slightly higher intensity than does the aqueous polymer solution. Similar results have also been reported by Ptasinski et al. [34]. Axial turbulent intensity is also higher around the outer pipe wall, a result which has also been reported in previous studies [27, 39]. Results of the DNS work of drag reduction in channel flows also indicate a slight reduction of axial intensities in the immediate vicinity of the walls [40]. Further away from the wall, however, polymer shows higher intensity around the outer pipe wall. This is also consistent with previous studies [15, 17, 39]. Although Warholic et al. [36] have reported that for cases of high drag reduction, axial intensity decreases, for low drag reduction cases it is shown that axial intensity always increases [15, 17].

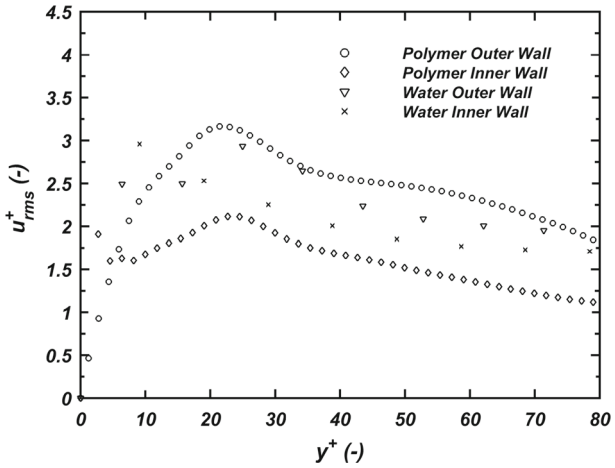

Fig. 24 Axial intensity profile at $\mathbf{Re_s} = \mathbf{66400}$

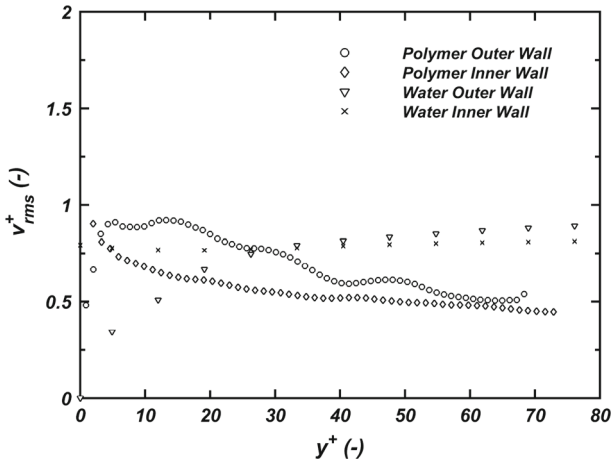

Fig. 25 Radial intensity profile at $\mathbf{Re_s} = \mathbf{47000}$

The peak of turbulence intensity seems to take place at a dimensionless distance of about 20 wall units. Numerical studies have shown that maximum polymer molecule extension takes place at approximately 20 wall units [34]. In the recoil of stretched polymer molecules, they cause a higher axial intensity, ultimately causing higher turbulence intensity in the buffer layer [34, 35]. Although the peak intensity is higher for the polymer, after a distance of about 70 wall units the turbulence intensity of the polymer drops to a level lower than that of water. According to Ptasinski et al. [34], the existence of a shear sheltering layer causes an increase in the level of axial intensity in the buffer layer by amplifying the axial fluctuation velocity the addition of the polymer also thickens the buffer layer.

The addition of the polymer causes the peak of axial velocity fluctuation to move away from the wall [41]. In this regard, DNS work conducted by Sureshkumar et al. [41] has shown that axial intensity increases in the buffer layer for polymer solution while

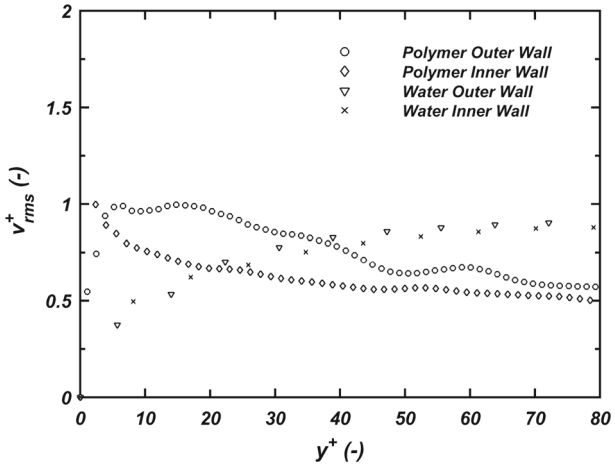

Fig. 26 Radial intensity profile at $\mathbf{Re_s} = \mathbf{57000}$

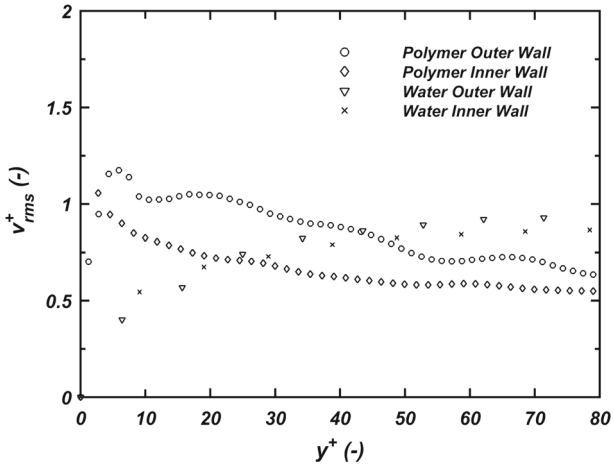

Fig. 27 Radial intensity profile at $\mathbf{Re_s = 66400}$

wall-normal and spanwise velocity fluctuations decease. They have argued that, by using Prandtl's mixing length, it is possible to explain the increase of axial turbulent intensity. According to Sureshkumar et al. [41], $u_{rms} \sim y(\frac{du}{dy})$, and it is known that, in the viscous sublayer, velocity correlates linearly with distance, i.e., $\left(\frac{du}{dy}\right) = 1$. In the case of viscoelastic fluids, the viscous sublayer is several times thicker, which results in higher u_{rms} near the walls than for Newtonian fluids, (i.e., the value of y for cases in which linear velocity correlation applies is larger for polymer solutions). Away from the wall, however, u_{rms} becomes the same for both types of fluids. This is consistent with the present experimental results.

6.4.2 Radial intensities

Similar to axial intensity, radial intensities are defined and normalized as follows:

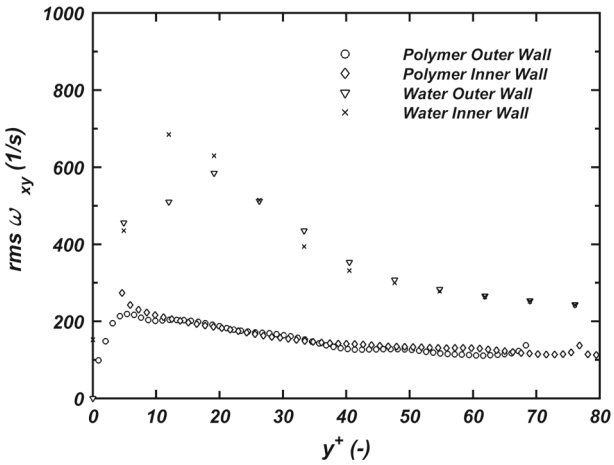

Fig. 28 RMS of vorticity for water and 0.175 % polymer solution at $\mathbf{Re_s = 47000}$

$$v^{+}_{rms} = \frac{V_{RMS}}{u_\tau} \tag{25}$$

Figures 25, 26, and 27 show the radial intensity profiles in the wall units. Although for $y^+ < 11$ the polymer shows slightly higher values of radial intensity, it is subsequently reduced significantly for the aqueous polymer solution. The reduction of radial intensity as a result of the addition of the polymer has been reported in previous studies as well [1, 15, 17, 34, 35]. The experimental results of Warholic et al. [36] have confirmed that the addition of polymer to the flow causes the flow to become more parallel to the wall, which implies less fluctuation in the radial direction. According to Lumley [33], polymer molecules in the buffer layer suppress the radial turbulent intensities. In fact, the reduction of the radial component of fluctuation velocity is the main reason for the significant decrease in Reynolds stress.

The phenomenon by which the polymer solution shows higher radial turbulence intensity in the viscous sublayer can be explained using the results of numerical work carried out by Sibilla et al. [42]. In the viscous sublayer polymer chains tend to orient in a vertical plane with respect to the streamwise direction, whereas in the buffer layer their preferred orientation is streamwise [42]. In other words, in the buffer layer, polymer chains tend to be parallel to the wall, as has also been reported by Warholic et al. [37]. This causes the radial and spanwise velocity fluctuation to be dampened while the axial intensity is magnified. In the viscous sublayer the orientation is different and therefore an amplification of radial velocity fluctuation is expected. Also it is worth mentioning that, according to Sibilla et al. [42], after $y^+ = 70$, polymer chains lose their preferred orientation and the flow becomes isotropic.

6.5 RMS of vorticity fluctuations

The RMS of vorticity fluctuations shows the strength of near-wall vortices [38], where higher RMS values of vorticity fluctuations results in a higher wall shear stress. Drag reduction occurs as a result of a reduction in the RMS of vorticity fluctuations [40, 41]. Figures 28, 29, and 30 show the calculated values of RMS of axial vorticity fluctuations for water and the polymer fluid. 2-D vorticity is calculated from the instantaneous velocity

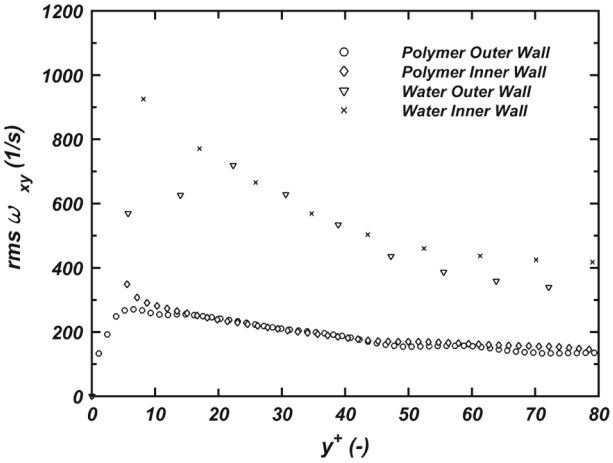

Fig. 29 RMS of vorticity for water and 0.175 % polymer solution at $\mathbf{Re_s = 57000}$

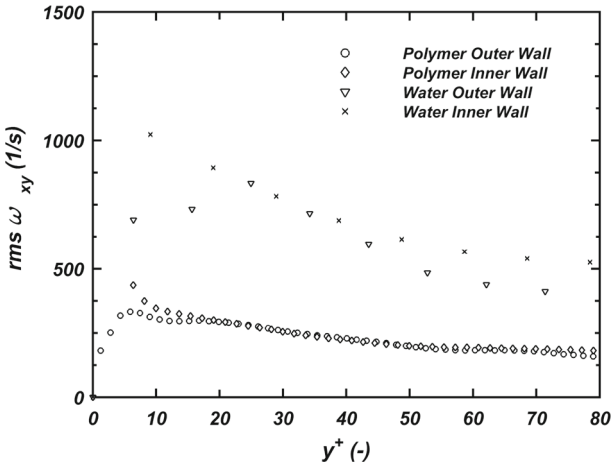

Fig. 30 RMS of vorticity for water and 0.175 % polymer solution at $\mathbf{Re_s = 66400}$

field according to Eq. 26.

$$\omega_{xy} = \frac{dv}{dx} - \frac{du}{dy} \tag{26}$$

The RMS of vorticity fluctuations is then calculated from the 2-D vorticity data.

Figures 28, 29 and 30 report the RMS of vorticity fluctuations for water and 0.175 % polymer solution. A clear reduction in the RMS of vorticity is observed for the aqueous polymer solution, suggesting weaker vortical activity for the polymer case. According to results from the DNS work of Min et al. [40], a significant reduction in the RMS of axial vorticity occurs as a result of drag reduction. The addition of polymers causes vorticity to relocate its peak further away from the solid walls. This relocation therefore weakens the sweep motions in the boundary layer, which ultimately results in reducing the wall shear stress [40]. Similar results have been reported by Sureshkumar et al. [41]. They argued that significant reduction in RMS of vorticity causes an increase in the average size of wall eddies, in turn implying a reduction in the generation of coherent structures of sweep motion and ultimately drag reduction [41]. Sibilla et al. [42] showed that polymer causes an increase in the size of near-wall vortices, which in turn reduces their strength.

7 Conclusions

Flow of a shear thinning polymer fluid has been studied in a concentric annulus with a radius ratio of 0.4. The aqueous polymer solutions have been found to exhibit rheological behavior which can be characterized by the Carreau rheology model with strong shear thinning behavior.

The $f - Re$ data for flow of aqueous polymer solutions fell close to the correlation of Newtonian fluids in the laminar regime. In the turbulent regime, a reduction in friction factor was observed. The critical Reynolds number was found to be above 3,000.

Mean axial velocity of polymer fluids has shown good agreement with the universal law of the wall in the immediate vicinity of the wall ($y^+ < 11$), while an upward shift of the axial velocity profile has been observed in the logarithmic zone ($y^+ > 11$). Velocity profiles

in the logarithmic region tended to shift toward the ultimate asymptote of drag reduction consistent with pipe flow.

The Reynolds stresses for polymer fluid flow decreased with increasing polymer concentration and were found to be much lower than those for water. The main reason for this phenomenon was the reduction in the radial component of the fluctuation velocity. Polymer stress was roughly quantified at the solid walls and was found to have a significant contribution to total stress. A higher stress deficit was observed to exist around the inner wall than near the outer wall. The radial position of maximum velocity for the 0.175 % polymer solution was slightly greater than that of water and was independent of Reynolds number.

Higher axial turbulence intensities were observed near the outer pipe wall of the annuli. The peak of the axial intensity was located in the buffer zone. Within the buffer layer, axial intensities were slightly higher for polymer fluids than for water around the outer pipe wall. Beyond a distance of about 70 wall units, the axial intensities of the polymer fluid dropped to a level lower than those of the water. Radial turbulence intensities were lower for polymer fluid (0.175 %) than for water, with the exception of the regions near the walls.

Comparison of the RMS values of the axial vorticity fluctuations showed a significant reduction in the case of the polymer solution. This is consistent with results from previous studies, suggesting that a reduction in the strength of near-wall vortices causes a decrease in coherent structures (sweep and bursts).

Nomenclature

R_2	Inner Radius of outer pipe (mm)
R_1	Outer Radius of inner pipe (mm)
R_0	Radius of zero shear stress (mm)
R_{max}	Radius of maximum velocity (mm)
R	Radius (mm)
D_H	Hydraulic Diameter (mm)
D_o	Outer pipe diameter (mm)
D_i	Inner pipe diameter (mm)
y	Distance from wall (mm)
L	Pipe length (m)
A	Annular area cross section (m^2)
G′	Elasticity (storage) modulus (Pa)
G″	Viscous (loss) modulus (Pa)
F	Frequency (Hz)
δ	Phase angle ($degree$)
C	Volumetric Concentration (%)
Q	Flow Rate ($\frac{m^3}{s}$)
U	axial velocity ($\frac{m}{s}$)
f	Fanning Friction Factor (-)
$\frac{dp}{dx}$	Frictional Pressure Drop ($\frac{Pa}{m}$)
Δt	Time between two cameras frame (s)
Δs	Displacement of tracer particles (m)
Δx	Axial displacement of tracer particles (m)
Δy	Radial displacement of tracer particles (m)
Re	Reynolds Number ($-$)

$\mathrm{Re_s}$	Solvent Reynolds number $(-)$
U_B	Bulk Velocity $(\frac{m}{s})$
ρ	Solution Density $\left(\frac{Kg}{m^3}\right)$
τ	Total Shear Stress (Pa)
$\dot{\gamma}$	Shear rate $(\frac{1}{s})$
τ_v	Viscous stress for flow of water (Pa)
τ_A	Average wall shear stress (Pa)
τ_i	Wall shear stress on inner wall (Pa)
τ_o	Wall shear stress on outer wall (Pa)
τ_{Re}	Reynolds stress (Pa)
τ_s	Solvent shear stress (Pa)
τ_p	Polymer stress (Pa)
$u^{'}$	Axial Fluctuation Velocity $(\frac{m}{s})$
$v^{'}$	Radial Fluctuation Velocity $(\frac{m}{s})$
n	Flow Behavior Index (-)
η	Apparent Viscosity $(Pa.\,s)$
η_w	Viscosity at the Wall $(Pa.s)$
η_s	Solvent viscosity $(Pa.s)$
u_τ	Shear Velocity $(\frac{m}{s})$
y^+	Dimensionless Distance $(-)$
u^+	Dimensionless Velocity $(-)$
ξ	Dimensionless Radial Location $(-)$
ξ_{max}	Dimensionless radial location of maximum velocity (-)
U_{RMS}	Root Mean Square of axial fluctuation velocity $(\frac{m}{s})$
V_{RMS}	Root Mean Square of radial fluctuation velocity $(\frac{m}{s})$
u^+_{RMS}	Dimensionless axial turbulent intensity $(-)$
v^+_{RMS}	Dimensionless radial turbulent intensity $(-)$
ω_{xy}	2-D vorticity $(\frac{1}{s})$
$rms\omega_{xy}$	RMS of vorticity fluctuations $(\frac{1}{s})$

Acknowledgments This research is financially supported through the funds available from Natural Sciences and Engineering Research Council of Canada (NSERC RGPAS 411966 KURU and NSERC RGPIN 238623 KURU). The authors wish to thank Canamara United for providing the polymer used in this study (Alcomer 110RD).

References

1. Pinho, F.T., Whitelaw, J.H.: Flow of Non-Newtonian Fluids in a Pipe. J. Non-Newtonian Fluid Mech. **34**(2), 129–144 (1990)
2. Escudier, M.P., Rosa, S., Poole, R.J.: Asymmetry in transitional pipe flow of drag-reducing polymer solutions. J. Non-Newtonian Fluid Mech. **161**(1–3), 19–29 (2009)
3. Japper-Jaafar, A., Escudier, M.P., Poole, R.J.: Turbulent pipe flow of a drag-reducing rigid "rod-like" polymer solution. J. Non-Newtonian Fluid Mech. **161**(1–3), 86–93 (2009)
4. Fredrickson, A.G., Bird, R.B.: Non-Newtonian Flow in Annuli. Ind. Eng. Chem. **50**(3), 347–352 (1958)
5. Hanks, R.W., Larsen, K.M.: Flow of Power-Law Non-Newtonian Fluids in Concentric Annuli. Ind. Eng. Chem. Fundam. **18**(1), 33–35 (1979)
6. Clump, C.W., Kwasnosk, D.: Turbulent Flow in Concentric Annuli. AIChE J **14**(1), 164–168 (1968). doi:10.1002/aic.690140128
7. Dodge, D.W., Metzner, A.B.: Turbulent Flow of Non-Newtonian Systems. AIChE J **5**(2), 189–204 (1959)

8. Colebrook, C.R.: Turbulent flow in pipes with particular reference to the transition region between the smooth and rough pipe laws. J. Inst. Civ. Eng. (London) **11**(4), 133–156 (1939). doi:10.1680/ijoti.1939.13150
9. Kundu, P.K., Cohen, I.M. Fluid mechanics, 4th ed., vol. XXVIII, p. 872 S. Elsevier, Amsterdam (2008)
10. Rothfus, R.R., Monrad, C.C., Senecal, V.E.: Velocity distribution and fluid friction in smooth concentric annuli. Ind. Eng. Chem. **42**(12), 2511–2520 (1950)
11. Lawn, C.J., Elliott, C.J.: Fully developed turbulent-flow through concentric annuli. J. Mech. Eng. Sci. **14**(3), 195–204 (1972)
12. Brighton, J.A., Jones, J.B.: Fully developed turbulent flow in annuli. J. Basic Eng. **86**, 835–842 (1964)
13. Ahn, S.W., Kim, K.C.: Characteristics of turbulent flow in the annuli with smooth and rough surfaces. KSME Int. J. **13**(2), 183–190 (1999)
14. Jones, O.C., Leung, J.C.M.: An Improvement in the calculation of turbulent friction in smooth concentric annuli. J. Fluids Eng.-Trans. ASME **103**(4), 615–623 (1981)
15. Nouri, J.M., Umur, H., Whitelaw, J.H.: Flow of newtonian and non-newtonian fluids in concentric and eccentric annuli. J. Fluid Mech. **253**, 617–641 (1993)
16. Escudier, M.P., Gouldson, I.W., Jones, D.M.: Flow of shear-thinning fluids in a concentric annulus. Exp. Fluids **18**(4), 225–238 (1995)
17. Japper-Jaafar, A., Escudier, M.P., Poole, R.J.: Laminar, transitional and turbulent annular flow of drag-reducing polymer solutions. J. Non-Newtonian Fluid Mech. **165**(19–20), 1357–1372 (2010)
18. Virk, P.S., Mickley, H.S., Smith, K.A.: Ultimate asymptote and mean flow structure in toms phenomenon. J. Appl. Mech. **37**(2), 488–493 (1970)
19. Bird, R.B., Armstrong, R.C., Hassager, O. Dynamics of polymeric liquids, 2nd ed., vol. 1. Wiley, New York (1987)
20. Hanks, R.W., Bonner, W.F.: Transitional flow phenomena in concentric annuli. Ind. Eng. Chem. Fundam. **10**(1), 105–113 (1971)
21. Dou, H.S., Khoo, B.C., Tsai, H.M.: Determining the critical condition for turbulent transition in a full-developed annulus flow. J. Pet. Sci. Eng. **73**(1–2), 41–47 (2010)
22. Rothfus, R.R., Sartory, W.K., Kermode, R.I.: Flow in Concentric Annuli at High Reynolds Numbers. AIChE J **12**(6), 1086–1091 (1966)
23. Walker, J.E., Rothfus, R.R.: Transitional Velocity Patterns in a Smooth Concentric Annulus. AIChE J **5**(1), 51–54 (1959)
24. Rehme, K.: Turbulent-Flow in Smooth Concentric Annuli with Small Radius Ratios. J. Fluid Mech. **64**(19), 263–287 (1974)
25. Chung, S.Y., Rhee, G.H., Sung, H.J.: Direct numerical simulation of turbulent concentric annular pipe flow - Part 1: Flow field. Int. J. Heat Fluid Flow **23**(4), 426–440 (2002). doi: 10.1016/S0142-727x(02)00140-6
26. Quarmby, A.: An experimental study of turbulent flow through concentric annuli. J. Mech. Sci. **9**(4), 205–221 (1967)
27. Rehme, K.: Turbulence measurements in smooth concentric annuli with small radius ratios. J. Fluid Mech. **72**(11), 189–206 (1975)
28. Poole, R.J.: Development-length requirements for fully developed laminar flow in concentric annuli. J. Fluids Eng. **132**(6), 64501 (2010). doi:10.1115/1.4001694
29. Wieneke, B.: Stereo-PIV using self-calibration on particle images. Exp. Fluids **39**(2), 267–280 (2005)
30. Melling, A.: Tracer particles and seeding for particle image velocimetry. Meas. Sci. Technol. **8**(12), 1406–1416 (1997)
31. Nezu, I., Sanjou, M.: PIV and PTV measurements in hydro-sciences with focus on turbulent open-channel flows. J. Hydro Environ. Res. **5**(4), 215–230 (2011)
32. Corredor, F.R.E., Bizhani, M., Ashrafuzzaman, M., Kuru, E.: An experimental investigation of turbulent flow in concentric annulus using particle image velocimetry technique. ASME J. Fluids Eng. (2013). FE-13-1642
33. Lumley, J.L.: Drag Reduction by Additives. Ann. Rev. Fluid Mech. **1**, 367–384 (1969)
34. Ptasinski, P.K., Boersma, B.J., Nieuwstadt, F.T.M., Hulsen, M.A., van den Brule, B.H.A.A., Hunt, J.C.R.: Turbulent channel flow near maximum drag reduction: simulations, experiments and mechanisms. J. Fluid Mech. **490**, 251–291 (2003)
35. Ptasinski, P.K., Nieuwstadt, F.T.M., van den Brule, B.H.A.A., Hulsen, M.A.: Experiments in turbulent pipe flow with polymer additives at maximum drag reduction. Flow Turbulence and Combustion **66**(2), 159–182 (2001). doi:10.1023/A: 1017985826227
36. Warholic, M.D., Massah, H., Hanratty, T.J.: Influence of drag-reducing polymers on turbulence: effects of Reynolds number, concentration and mixing. Exp. Fluids **27**(5), 461–472 (1999)

37. Warholic, M.D., Heist, D.K., Katcher, M., Hanratty, T.J.: A study with particle-image Velocimetry of the influence of drag-reducing polymers on the structure of turbulence. Exp. Fluids **31**(5), 474–483 (2001)
38. Paschkewitz, J.S., Dubief, Y., Dimitropoulos, C.D., Shaqfeh, E.S.G., Moin, P.: Numerical simulation of turbulent drag reduction using rigid fibres. J. Fluid Mech. **518**, 281–317 (2004)
39. Chung, S.Y., Sung, H.J.: Large-eddy simulation of turbulent flow in a concentric annulus with rotation of an inner cylinder. Int. J. Heat Fluid Flow **26**(2), 191–203 (2005). doi:10.1016/j.ijheatfluidflow.2004.08.006
40. Min, T., Jung, Y.Y., Choi, H., Joseph, D.D.: Drag reduction by polymer additives in a turbulent channel flow. J. Fluid Mech. **486**, 213–238 (2003). doi:10.1017/S0022112003004610
41. Sureshkumar, R., Beris, A.N., Handler, R.A.: Direct numerical simulation of the turbulent channel flow of a polymer solution. Physics of Fluids no **9**(3), 743–755 (1997). doi:10.1063/1.869229
42. Sibilla, S., Baron, A.: Polymer stress statistics in the near-wall turbulent flow of a drag-reducing solution. Phys. Fluids **14**(3), 1123–1136 (2002)